

DIELECTRICS

Ultrahigh energy storage in superparaelectric relaxor ferroelectrics

Hao Pan^{1†}, Shun Lan^{1†}, Shiqi Xu², Qinghua Zhang³, Hongbao Yao³, Yiqian Liu¹, Fanqi Meng¹, Er-Jia Guo³, Lin Gu³, Di Yi¹, Xiao Renshaw Wang⁴, Houbing Huang², Judith L. MacManus-Driscoll⁵, Long-Qing Chen⁶, Kui-Juan Jin^{3*}, Ce-Wen Nan^{1*}, Yuan-Hua Lin^{1*}

Electrostatic energy storage technology based on dielectrics is fundamental to advanced electronics and high-power electrical systems. Recently, relaxor ferroelectrics characterized by nanodomains have shown great promise as dielectrics with high energy density and high efficiency. We demonstrate substantial enhancements of energy storage properties in relaxor ferroelectric films with a superparaelectric design. The nanodomains are scaled down to polar clusters of several unit cells so that polarization switching hysteresis is nearly eliminated while relatively high polarization is maintained. We achieve an ultrahigh energy density of 152 joules per cubic centimeter with markedly improved efficiency (>90% at an electric field of 3.5 megavolts per centimeter) in superparaelectric samarium-doped bismuth ferrite-barium titanate films. This superparaelectric strategy is generally applicable to optimize dielectric and other related functionalities of relaxor ferroelectrics.

Compared with electrochemical energy storage techniques, electrostatic energy storage based on dielectric capacitors is an optimal enabler of fast charging-and-discharging speed (at the micro-second level) and ultrahigh power density (1–3). Dielectric capacitors are thus playing an ever-increasing role in electronic devices and electrical power systems. However, the relatively low energy storage densities of dielectric capacitors have hindered their broader applications, for which device miniaturization, system compactness, and cost reduction are required. Extensive efforts have thus been focused on developing reliable and efficient dielectrics with higher energy densities (4, 5).

Energy storage in dielectrics is realized via dielectric polarization P in an external electric field E , with the energy density U_e determined by $\int_{P_r}^{P_m} E dP$, where P_m and P_r are the maximum polarization in the charging process and remnant polarization in the discharging process, respectively (fig. S1) (6). P_r manifests itself as the P - E hysteresis, which not only limits the achievable U_e but generates noticeable energy loss U_{loss} , degrading the efficiency

η [defined as $U_e/(U_e + U_{\text{loss}})$] and causing an energy (heat) dissipation problem in practical uses (7). High U_e and η are thus to be achieved by realizing large polarization (P_m) and small hysteresis (P_r and U_{loss}) (6–8). The main approach to improving the polarization and energy performances has been to develop relaxor ferroelectrics (RFEs) from ferroelectric nonlinear dielectrics—e.g., $\text{Pb}(\text{Zr,Ti})\text{O}_3$ (PZT) and BiFeO_3 that have strong P_m but unwanted large hysteresis due to their characteristic polar domains and large energy barriers in domain switching (6, 9). By ion doping and/or solid solution in ferroelectrics, the long-range-ordered micrometer-size ferroelectric domains are transformed into short-range-ordered nanodomains with increased local heterogeneity in RFEs (10–12). Shrinking domain size and weakening domain intercoupling reduce the domain switching energy barriers, resulting in smaller hysteresis and enhancing U_e and η in RFEs (13). Representative examples include La-doped PZT RFE films with a U_e of 85 J cm^{-3} and a η of 65% (14), BiFeO_3 - BaTiO_3 - SrTiO_3 (BFO-BTO-STO) films with 112 J cm^{-3} and 80% (4), and $\text{Pb}(\text{Mg}_{1/3}\text{Nb}_{2/3})\text{O}_3$ - PbTiO_3 (PMN-PT) films with 133 J cm^{-3} and 75% (5).

RFEs are characterized by a diffuse phase transition over a broad temperature range, from the Burns temperature T_B at which nanodomains appear, to the intermediate temperature T_m at which nanodomains grow and the dielectric constant reaches the maximum, and finally to the freezing temperature T_f at which nanodomains become frozen (15). Investigations of RFE dielectrics mostly focus on the temperature (T) range of $T_f < T < T_m$, which sustains large P_m but still visible hysteresis (P_r and U_{loss}) accompanying the nanodomain switching (4, 5). The visible hysteresis has become a bottleneck for further improvement of U_e and η . To this end, designing RFEs in the

$T_m < T < T_B$ range, which are also defined as superparaelectric (SPE) RFEs (16), is a promising but scarcely explored approach. In the SPEs, nanodomains are further scaled down and domain intercoupling is further weakened to the level that domain switching energy barriers become comparable with or below the thermal disturbance energy kT (k is the Boltzmann constant) (17). The polarization of nanodomains can thus flip among energy-equivalent directions with high dynamics, which makes it possible to realize minimal hysteresis (18, 19). Theoretical calculations have predicted SPE features in temperature-driven and spatially confined nanograins (20). But experimental attempts on nanograin dielectrics show seriously depressed P_m because of the overwhelming amorphous matrix where the nanograins are embedded (21). By contrast, the temperature-driven SPE in RFEs has been found to maintain nonlinear polarization with high P_m while achieving minimized hysteresis (22), which is desirable to realize both high U_e and η in dielectric capacitors.

To demonstrate the effectiveness of the temperature-driven SPE design for enhancing the dielectric energy storage performance, we first conducted phase-field simulations (23). We simulated a series of compositions for 10 mol % Sm-doped $y\text{BFO}$ -(1 - y) BTO (Sm-BFBT; $y = 0.1$ to 0.9). We used the BFO-BTO system because it is a promising RFE with high P_m (9, 24). We adopted the Sm dopant because it is efficient at increasing local heterogeneity (25), which helps to achieve SPE features in RFEs. We simulated temperature-dependent dielectric constants, domain structures, and P - E loops of Sm-BFBT (figs. S2 to S4). Our simulation results display similar temperature-dependent evolutions that are typical of RFEs and agree well with the nanodomain model. The composition with $y = 0.3$ (Fig. 1A), for example, exhibits a typical dispersed dielectric constant-temperature curve with a broad phase transition peak and characteristic temperatures T_f , T_m , and T_B . We observed features of ferroelectrics, conventional RFEs, SPE RFEs, and paraelectrics at the $T < T_f$, $T_f < T < T_m$, $T_m < T < T_B$, and $T > T_B$ ranges, respectively (Fig. 1B). Compared with the large average domain size of $\sim 26 \text{ nm}$ in the ferroelectric (at 200 K) and $\sim 10 \text{ nm}$ in the conventional RFE (at 450 K), we found a much smaller domain size in the SPE ($\sim 1.5 \text{ nm}$ at 800 K). The P - E loop is simultaneously slimmed to a notable degree, resulting in a minimal hysteresis for the SPE. The SPE sustains a moderate polarization reduction due to the emergence of a nonpolar phase and a decrease of the domain fraction. However, compared with the paraelectric (at 1100 K) that has negligible hysteresis but linear-type polarization due to the elimination of polar domains, the SPE retains dielectric

¹State Key Laboratory of New Ceramics and Fine Processing, School of Materials Science and Engineering, Tsinghua University, Beijing 100084, China. ²Advanced Research Institute of Multidisciplinary Science, Beijing Institute of Technology, Beijing 100081, China. ³Beijing National Laboratory for Condensed Matter Physics, Institute of Physics, Chinese Academy of Sciences, Beijing 100190, China. ⁴School of Physical and Mathematical Sciences, Nanyang Technological University, 637371 Singapore, Singapore. ⁵Department of Materials Science and Metallurgy, University of Cambridge, 27 Charles Babbage Road, Cambridge CB3 0FS, UK. ⁶Department of Materials Science and Engineering, Materials Research Institute, The Pennsylvania State University, University Park, PA, USA. *Corresponding author. Email: kjiin@iphy.ac.cn (K.-J.J.); cwnan@mail.tsinghua.edu.cn (C.-W.N.); linyh@tsinghua.edu.cn (Y.-H.L.) †These authors contributed equally to this work.

Fig. 1. Phase field simulations of the SPE design in RFEs for high-performance dielectric energy storage. (A) Simulated temperature-dependent dielectric constant of the RFE with a composition of 10 mol % Sm-doped $y\text{BFO}-(1-y)\text{BTO}$ (Sm-BFBT; $y = 0.3$). T_1 to T_4 are the temperature segments divided by the characteristic T_f , T_m , and T_B values. a.u., arbitrary units. (B) Simulations of the domain structures and P - E loops at 200, 450, 800, and 1100 K of Sm-BFBT with $y = 0.3$, showing ferroelectric (FE), conventional RFE, SPE-RFE, and paraelectric (PE) features, respectively. The simulation size is 128 nm by 128 nm by 16 nm. The blue area represents the nonpolar phase; other colored areas indicate domains with various polarization directions. The shaded areas in the P - E loops represent the energy density. (C and D) Simulated two-dimensional distributions of (C) the energy density U_e and efficiency η and (D) the U_F parameter of Sm-BFBT with respect to domain size and fraction. The upper-left and lower-right blank areas are thermodynamically unstable regions where data are not collected. The arrowed curve shows the temperature-dependent evolution of Sm-BFBT with $y = 0.3$.

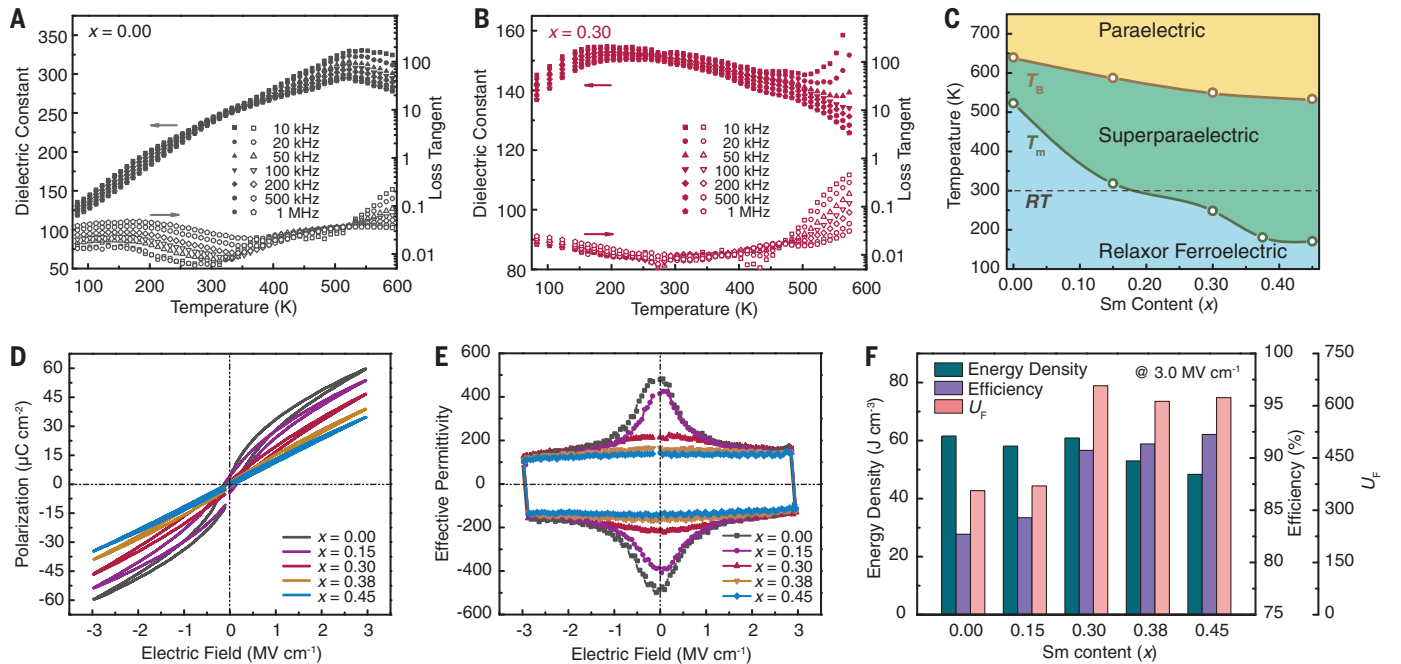
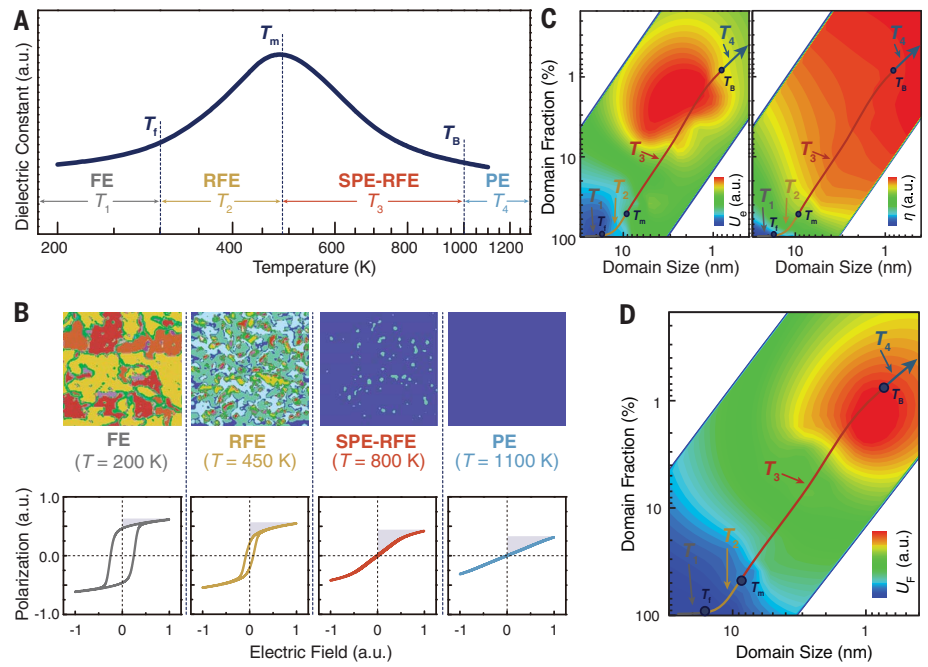


Fig. 2. Dielectric, polarization, and energy storage properties of the Sm-BFBT films. (A and B) Temperature-dependent dielectric spectra for (A) $x = 0$ and (B) $x = 0.30$. (C) Phase diagram of the Sm-BFBT films with respect to temperature and Sm content x . RT denotes room temperature. T_m values are derived from the

dielectric spectra at 1 MHz; T_B values are from SHG measurements. (D) P - E loops at an electric field of 3.0 MV cm^{-1} and 5 kHz. (E) Field-dependent effective permittivity of the Sm-BFBT films. (F) Comparison of energy density, efficiency and U_F (unit: Joules per cubic centimeter) of the Sm-BFBT films at 3.0 MV cm^{-1} .

nonlinearity and relatively high P_m (Fig. 1B), thus achieving the best compromise for energy storage.

To quantitatively evaluate the trade-off between high polarization (large U_e) and low hysteresis (low U_{loss} and thus high η) for high overall energy storage performance, we defined

a parameter $U_F = U_e / (1 - \eta)$. From the simulated P - E loops of Sm-BFBT (fig. S4), we derived the U_e and η values and calculated U_F . We displayed U_e , η , and U_F as two-dimensional distributions for the domain size and fraction (Fig. 1, C and D). We found that a high U_e could be attained with moderate domain sizes

of 1 to 10 nm and moderate domain fractions of 0.5 to 8%, whereas η is monotonously increased with reduced domain size and fraction. The area with high U_F is thus driven to the ranges with a domain size of < 2 nm (two to five unit cells for the perovskite Sm-BFBT) and domain fraction of ~ 0.5 to 5%, which are

characteristic of SPE. The curve denoting the temperature-driven domain evolution for $y = 0.3$ is also shown, on which the largest U_e , high η , and best U_F lie in the SPE ($T_m < T < T_B$) segment rather than the conventional RFE ($T_f < T < T_m$) range (Fig. 1, C and D).

Because the SPE appears at temperatures above T_m , which is usually high [e.g., ~ 430 K for BFO-BTO-STO (4) and ~ 410 K for PMN-PT (25)], realizing room temperature SPE dielectrics is important for practical applications. We judiciously controlled the Sm doping ratio (x) in the 30BFO-70BTO films. The Sm ions doped into the A sites of a perovskite ABO_3 lattice can bring in strong local chemical, structural, and electrical heterogeneities (25). These factors interrupt the ferroelectric order, scale down the nanodomain size, and thus efficiently modulate the SPE segment to room temperature (26, 27). We fabricated a series of Sm-BFBT films with $x = 0, 0.15, 0.30, 0.38,$ and 0.45 via pulsed laser deposition on (001)-oriented Nb-doped STO substrates (23). All samples are epitaxial films with thicknesses of ~ 650 nm, as confirmed by x-ray diffraction (fig. S5), re-

ciprocal space mapping (fig. S6), and scanning transmission electron microscopy (STEM) (fig. S7). We measured the temperature-dependent dielectric spectra of Sm-BFBT films (Fig. 2, A and B, and fig. S8). As x increases, the films exhibit enhanced relaxor features, with decreased T_m values (523 K for $x = 0$ and 248 K for $x = 0.30$ at 1 MHz, respectively), more diffuse phase transitions, and weaker temperature dependence of the dielectric constant (28). The frequency dispersion—i.e., the difference of T_m at the frequencies of 1 MHz and 10 kHz—is also markedly increased from <5 K for $x = 0$ to ~ 48 K for $x = 0.30$. The relaxor diffuseness factor γ (derived from the modified Curie-Weiss law; fig. S9) also exhibits an increasing trend as x increases: $\gamma = 1.2, 1.6,$ and 1.7 for $x = 0, 0.30,$ and 0.45 , respectively. The dielectric loss tangent over a wide temperature and frequency range shows a tendency to decline as x increases, which is also associated with the enhanced relaxor properties and easier nanodomain switching in the SPE films (29). With the T_m values from the dielectric spectra at 1 MHz and T_B values from second

harmonic generation (SHG) measurements (discussed later), a phase diagram can be built (Fig. 2C). The T_m values decrease substantially with increased Sm content, which facilitates the transition from RFE to SPE. As a result, though Sm-BFBT films with $x = 0$ and 0.15 remain conventional RFEs at the room temperature, a crossover to SPE occurs as x increases further.

We measured P - E loops of the Sm-BFBT films at an electric field of 3.0 MV cm^{-1} and 5 kHz (Fig. 2D) to characterize the high-voltage dielectric polarization and energy storage properties. The film with $x = 0$ shows typical RFE features with a strong P_m of 60 $\mu\text{C cm}^{-2}$ but a visible P_r of 6.3 $\mu\text{C cm}^{-2}$ and a U_{loss} of 13 J cm^{-3} . We found similar RFE features for $x = 0.15$ (table S1). As we increased x to 0.30 , P_r and U_{loss} were substantially reduced to 2.5 $\mu\text{C cm}^{-2}$ and 6 J cm^{-3} , respectively, while a high P_m of 47 $\mu\text{C cm}^{-2}$ was maintained. This indicates the transition from RFE to SPE, which is more distinctly illustrated by the electric field-dependent effective permittivity $dP/(dE \cdot \epsilon_0)$, where ϵ_0 is the vacuum permittivity (Fig. 2E). We observed high effective permittivity nonlinearity (the variation of the effective permittivity between 0 and 3.0 MV cm^{-1}) of 68% for the RFE ($x = 0$), which was reduced to 29% for the SPE ($x = 0.30$). The effective permittivity for $x = 0.30$ was noticeably suppressed at lower fields of <1 MV cm^{-1} but retained values of the same level as those for $x = 0$ at higher fields. This helps to delay polarization saturation while retaining large polarizability at high fields in SPE dielectrics, which is beneficial for energy storage. As a result, the RFE film with $x = 0$ achieves a high U_e of 62 J cm^{-3} but only a moderate η of 83% , and thus a low U_F of 356 (Fig. 2F). The SPE film with $x = 0.30$ shows a close U_e value of 61 J cm^{-3} , whereas η is markedly improved to 91% , giving rise to a U_F of 658 , which is 85% higher than that for $x = 0$. As x further increases to 0.45 , U_e declines to 48 J cm^{-3} owing to the reduction of P_m to 35 $\mu\text{C cm}^{-2}$ and the reduction of permittivity nonlinearity to 10% , but the ultrahigh η of $>92\%$ still contributes to a large U_F of 623 . These results are in good agreement with the simulations (Fig. 1), emphasizing the importance of the rational design of RFE dielectrics in the SPE segment for high energy storage performance.

We conducted SHG measurements of the Sm-BFBT films to shed light on the microstructural origins of the SPE. SHG is the process in which the base frequency ω of an incident light is doubled by a material with local inversion symmetry breaking (fig. S10). The technique is a sensitive probe for the evolution of polar structures (30), with the SHG intensity $I^{2\omega}$ proportional to the square of the polarization P ($I^{2\omega} \propto |P|^2$) (31). With increasing temperature, the SHG intensities gradually decrease in all of the films (Fig. 3A),

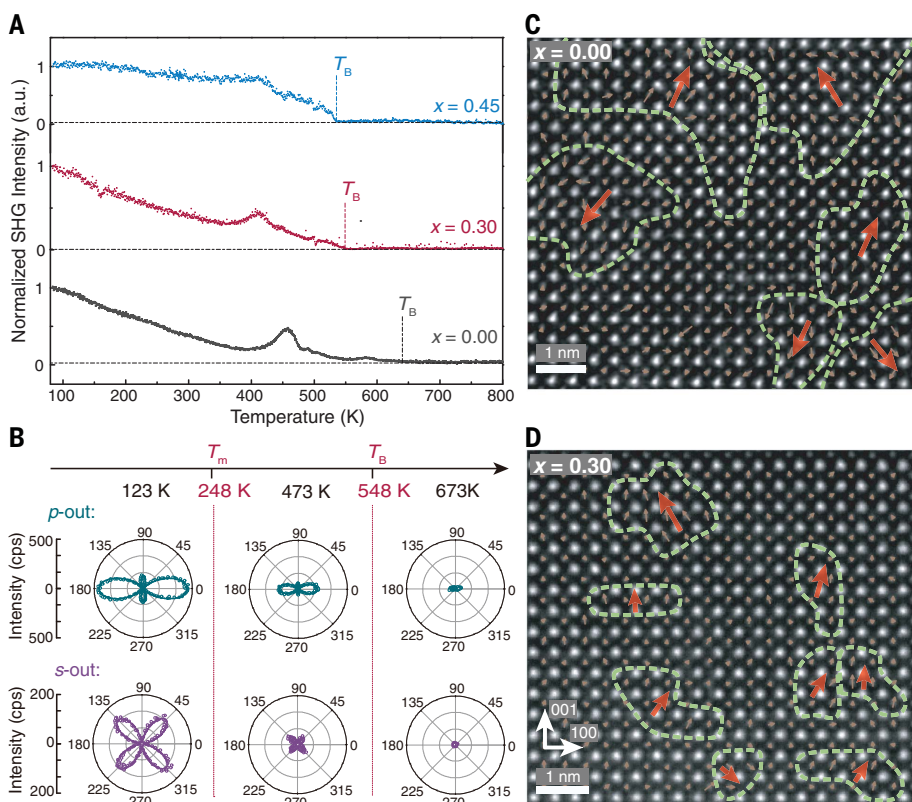


Fig. 3. Microstructural origins of the SPE. (A) Temperature-dependent SHG intensity (with the p -in and p -out configuration) of the Sm-BFBT films with $x = 0, 0.30,$ and 0.45 . (B) SHG patterns with the p -out and s -out configurations for $x = 0.30$ at $123, 473,$ and 673 K, corresponding to the RFE ($<T_m$), SPE ($T_m < T < T_B$), and paraelectric ($>T_B$) segments, respectively. Dots represent experimental data; lines represent fittings. (C and D) HAADF STEM images for (C) $x = 0$ and (D) $x = 0.30$. Brown arrows show B-site cation displacement vectors in each unit cell; green dashed lines delineate domain areas, in which red arrows denote the orientation of the collective B-site cation displacement of the domains.

indicating a decrease of domain fraction. The intensity anomalies above 400 K should be ascribed to thermally enhanced local disorder in the nanodomain structures, producing more domain walls that contribute to the SHG signal (32, 33). The SHG intensities reach minimal values (with only residual surface signals) at temperatures of 642, 548, and 533 K for $x = 0, 0.30,$ and $0.45,$ respectively, which were determined as the characteristic T_B above which the nanodomains are eliminated. These T_B values are much higher than the T_m determined from dielectric spectra (523, 248, and 171 K for $x = 0, 0.30,$ and 0.45 at 1 MHz, respectively). The persistence of SHG intensity in the $T_m < T < T_B$ segment indicates that polar domain structures remain in the SPE films. We also measured the angle-dependent SHG patterns (with p -out and s -out configurations in which the analyzer polarization was parallel and vertical, respectively, to the light incidence plane; fig. S10) of the Sm-BFBT films at representative temperatures in the RFE, SPE, and PE segments for $x = 0.30$ (Fig. 3B) and $x = 0$ and 0.45 (fig. S11). The films exhibit weaker but similar SHG patterns in the SPE segment relative to those of the RFE, whereas minimal intensity with disappearance of anisotropy is found in the paraelectric segment.

We made more direct characterizations of the nanodomains in the Sm-BFBT films with high-resolution high-angle annular dark-field (HAADF) STEM (Fig. 3, C and D). The local polarization within the ABO_3 lattice can be determined on the basis of the displacement of B-site cations (Fe/Ti with weaker contrast) relative to the center of the four nearest A-site cations (Ba/Bi/Sm with stronger contrast) (34). The domains in which the displacement vectors have the same direction are delineated. For $x = 0,$ the film exhibits typical nanodomain structures with diameters of ~ 2 to 5 nm and domain volume fraction of $\sim 54\%$. This configuration is similar to the results in typical RFEs (4), enabling us to interpret its polarization nonlinearity and hysteresis. For $x = 0.30$ (Fig. 3D), the nanodomains shrink to polar clusters of several unit cells, with average sizes of ~ 1 to 2 nm; the domain fraction decreases to $\sim 15\%$, whereas the nonpolar areas increase relative to those for $x = 0.$ This evolution is linked to the further destabilization of polar order with the strong local heterogeneity introduced by Sm doping. The observation of polar clusters clarifies the microstructural origin of the persistence of SHG intensity above T_m and the substantially suppressed hysteresis with relative high polarization in the SPE films.

To investigate the full potential of the Sm-BFBT films for energy storage, we obtained their statistical breakdown strengths E_b via Weibull distribution fitting (Fig. 4A). The E_b values of the films increase along with the

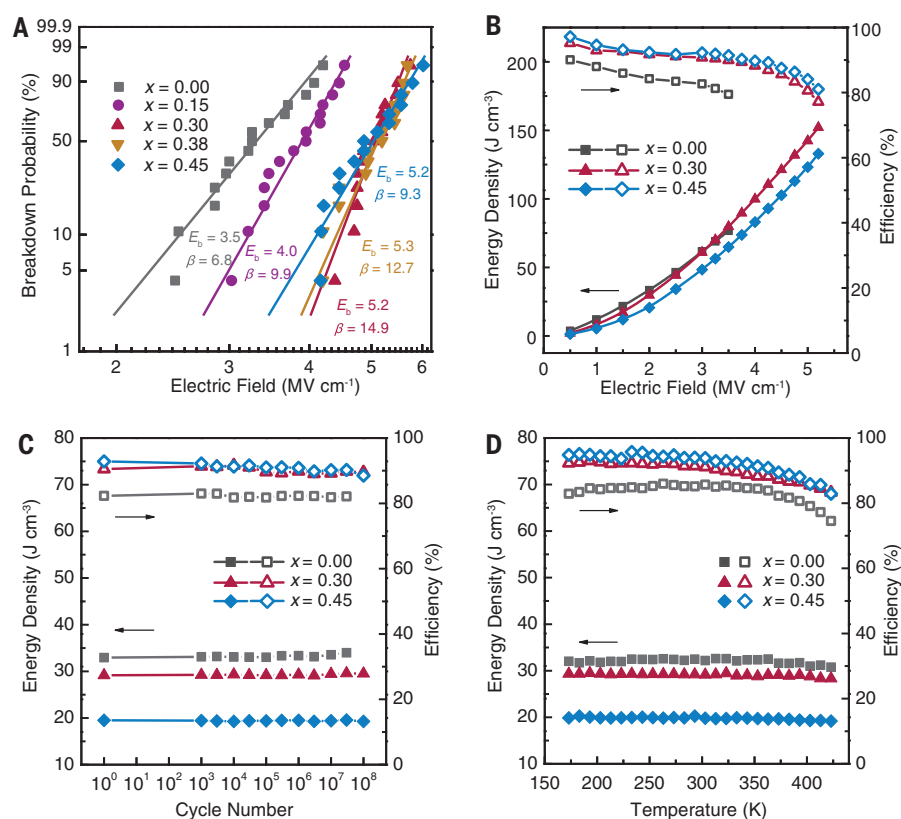


Fig. 4. Energy storage performance of the Sm-BFBT SPE films. (A) Two-parameter Weibull distribution analysis of the characteristic breakdown fields of the Sm-BFBT films. (B) Energy density and efficiency of the Sm-BFBT films as a function of electric field. (C) Energy storage performance of the films at an electric field of 2.0 MV cm^{-1} and 5 kHz with regard to the 20-kHz charging-and-discharging cycles. (D) Temperature dependence of energy storage performance of the films at an electric field of 2.0 MV cm^{-1} and 5 kHz over the temperature range of 173 to 423 K (T_m values for $x = 0, 0.30,$ and 0.45 are 523, 248, and 171 K, respectively).

Sm ratio—e.g., from $\sim 3.5 \text{ MV cm}^{-1}$ ($x = 0$) to $\sim 5.2 \text{ MV cm}^{-1}$ ($x = 0.30$ and 0.45). The Weibull modulus β also increases from 6.9 ($x = 0$) to 14.9 ($x = 0.30$) and 9.3 ($x = 0.45$), indicating narrowed distributions of E_b data and improved film uniformity (3). The substantial enhancement of the breakdown performance is directly ascribed to the prevention of electric and thermal breakdown of the films with the leakage current suppressed by more than one order of magnitude—e.g., from $8.2 \times 10^{-4} \text{ A cm}^{-2}$ ($x = 0$) to $3.0 \times 10^{-5} \text{ A cm}^{-2}$ ($x = 0.45$) at 2.0 MV cm^{-1} (fig. S12). We found that the leakage current of the Sm-BFBT films arose from combined contributions from bulk-limited Poole-Frenkel charge emission and interfacial-limited Schottky charge emission, especially at high fields (4) (fig. S13). We thus attribute the reduction of leakage current and improvement of E_b to the suppression of charge emission by Sm doping, with probable reduction of oxygen vacancies and formation of deep-level defect complexes (5) (supplementary text).

We derived the energy density U_e and efficiency η of the Sm-BFBT films at fields of up to their E_b (Fig. 4B and fig. S14) from the P - E loops at 5 kHz (fig. S15). The maximum U_e

(152 J cm^{-3}) was achieved in the SPE film with $x = 0.30,$ which represents a 97% improvement relative to the RFE film (77 J cm^{-3} for $x = 0$). U_e values of 139 and 133 J cm^{-3} were also obtained for $x = 0.38$ and $0.45,$ respectively. These ultrahigh U_e values in the SPE films are the combined results of high polarization, low hysteresis, and large $E_b.$ Moreover, compared with the moderate η value of $\sim 79\%$ (at 3.5 MV cm^{-1}) in the RFE film with $x = 0,$ a marked enhancement of η to $>90\%$ (at the same field) was achieved in the SPE films with $x \geq 0.30$ (Fig. 4B). The high η is critical to address the energy dissipation of dielectrics for high-power applications, facilitating reliable operation and suppressing unexpected failure. At fields approaching $E_b,$ η degrades as a result of increased conduction loss, which is common in high-field dielectrics (11). Even so, η values of $>77\%$ persist in the SPE films. The combined large U_e and high η in the Sm-BFBT films are competitive with those of the best lead-based RFE films (U_e of $133 \text{ J cm}^{-3}, \eta$ of 75%) (5), demonstrating the great promise of the Sm-BFBT SPE films as high-performance and environmentally friendly dielectrics.

In practical applications, reliability and stability of performance are also crucial for dielectric capacitors. During an accelerated charging-and-discharging test with a triangle field of 20 kHz and 2.0 MV cm^{-1} , the film with $x = 0$ breaks down after 3×10^7 cycles, whereas the SPE films with $x = 0.30$ and 0.45 survive over 1×10^8 cycles (fig. S16), with <5% degradations of both U_e and η (Fig. 4C). At a higher field of 3.0 MV cm^{-1} , the SPE film with $x = 0.30$ still maintains stable energy performances over 1×10^8 cycles (fig. S17). We ascribe this high reliability to the suppression of fatigue from domain wall pinning (35), benefiting from the highly dynamic polar cluster structures in the SPE films. The SPE films also exhibit good stability of polarization (fig. S18) and energy storage performance (Fig. 4D) over a wide temperature range (173 to 423 K), with U_e variation of <6% and η variation of <13%. This is associated with strong relaxor features in the SPE films, leading to temperature-insensitive dielectric properties. The slight decline of η at high temperatures is likely linked to the thermally stimulated conduction loss (2).

The temperature-driven SPE design of RFEs in the $T_m < T < T_B$ range, characterized by the reduction of nanodomain size to polar clusters of several unit cells, has been demonstrated to considerably enhance the overall dielectric energy storage performance. This strategy has a broad applicability to RFE-based energy storage dielectrics with various compositions and structures. The SPE design can also be

used to optimize other RFE-based functionalities for which minimized hysteresis is desired.

REFERENCES AND NOTES

- B. Chu *et al.*, *Science* **313**, 334–336 (2006).
- Q. Li *et al.*, *Nature* **523**, 576–579 (2015).
- H. Palneedi, M. Peddigari, G.-T. Hwang, D.-Y. Jeong, J. Ryu, *Adv. Funct. Mater.* **28**, 1803665 (2018).
- H. Pan *et al.*, *Science* **365**, 578–582 (2019).
- J. Kim *et al.*, *Science* **369**, 81–84 (2020).
- L. Yang *et al.*, *Prog. Mater. Sci.* **102**, 72–108 (2019).
- J. Li *et al.*, *Nat. Mater.* **19**, 999–1005 (2020).
- H. Huang, J. F. Scott, Eds., *Ferroelectric Materials for Energy Applications* (Wiley, 2018).
- S. Cho *et al.*, *Nano Energy* **45**, 398–406 (2018).
- H. Ogihara, C. A. Randall, S. Trolier-McKinstry, *J. Am. Ceram. Soc.* **92**, 1719–1724 (2009).
- H. Pan *et al.*, *Nat. Commun.* **9**, 1813 (2018).
- B. Peng *et al.*, *Adv. Electron. Mater.* **1**, 1500052 (2015).
- H. Pan, A. Kursumovic, Y.-H. Lin, C.-W. Nan, J. L. MacManus-Driscoll, *Nanoscale* **12**, 19582–19591 (2020).
- B. Ma *et al.*, *J. Mater. Sci. Mater. Electron.* **26**, 9279–9287 (2015).
- A. A. Bokov, Z.-G. Ye, *J. Adv. Dielectr.* **02**, 1241010 (2012).
- L. E. Cross, *Ferroelectrics* **76**, 241–267 (1987).
- A. J. Bell, *J. Phys. Condens. Matter* **5**, 8773–8792 (1993).
- Z. Yang *et al.*, *J. Mater. Chem. A* **7**, 27256–27266 (2019).
- F. Li, S. Zhang, D. Damjanovic, L.-Q. Chen, T. R. Shrout, *Adv. Funct. Mater.* **28**, 1801504 (2018).
- M. D. Glinchuk, E. A. Eliseev, A. N. Morozovska, *Phys. Rev. B* **78**, 134107 (2008).
- K. Wang *et al.*, *Adv. Energy Mater.* **10**, 2001778 (2020).
- A. E. Glazounov, A. J. Bell, A. K. Tagantsev, *J. Phys. Condens. Matter* **7**, 4145–4168 (1995).
- See supplementary materials.
- A. Kursumovic *et al.*, *Nano Energy* **71**, 104536 (2020).
- F. Li *et al.*, *Science* **364**, 264–268 (2019).
- D. Kan *et al.*, *Adv. Funct. Mater.* **20**, 1108–1115 (2010).
- M. Ganguly, S. K. Rout, W. S. Woo, C. W. Ahn, I. W. Kim, *Physica B* **411**, 26–34 (2013).
- V. V. Shvartsman, D. C. Lupascu, *J. Am. Ceram. Soc.* **95**, 1–26 (2012).
- G. Liu, S. Zhang, W. Jiang, W. Cao, *Mater. Sci. Eng. R Rep.* **89**, 1–48 (2015).
- S. A. Denev, T. T. A. Lummen, E. Barnes, A. Kumar, V. Gopalan, *J. Am. Ceram. Soc.* **94**, 2699–2727 (2011).
- M. Trassin, G. De Luca, S. Manz, M. Fiebig, *Adv. Mater.* **27**, 4871–4876 (2015).
- J. Wang *et al.*, *Appl. Phys. Lett.* **112**, 102904 (2018).
- B. Zalar, V. V. Laguta, R. Blinc, *Phys. Rev. Lett.* **90**, 037601–037601 (2003).
- A. K. Yadav *et al.*, *Nature* **530**, 198–201 (2016).
- J. Glaum, M. Hoffman, *J. Am. Ceram. Soc.* **97**, 665–680 (2014).

ACKNOWLEDGMENTS

We thank Z. Luo, Y. Zhang, and Y. Dong for fruitful discussions. **Funding:** This work was supported by the Basic Science Center Project of the National Natural Science Foundation of China (NSFC) grant 51788104 (Y.-H.L. and C.-W.N.); National Key Basic Research Program of China grant 2019YFA0308500 and NSFC grant 11721404 (K.-J.J.); NSFC grant 11974390 (E.-J.G.); NSFC grant 51729201 (Y.-H.L.); NSFC grants 52025025 and 52072400 (Q.Z. and L.G.); NSFC grant 51972028 (H.H.); Royal Academy of Engineering grant CIET 1819_24 (J.L.M.-D.); and US National Science Foundation (NSF) grant DMR-1744213 (L.-Q.C.). **Author contributions:** Y.-H.L., H.P., and S.L. conceived this study. H.P. and S.L. performed the experiments, with the supervision of Y.-H.L. and C.-W.N. S.X., H.H., and L.-Q.C. performed the phase-field simulations. H.P., S.L., and Y.L. fabricated the samples and carried out the electrical measurements. Q.Z., F.M., and L.G. performed the STEM characterizations. H.Y., E.-J.G., and K.-J.J. conducted the SHG measurement. H.P. wrote the first draft of the manuscript. All authors discussed the results and revised the manuscript. **Competing interests:** The authors declare that they have no competing interests. **Data and materials availability:** All relevant data are available in the main text or the supplementary materials.

SUPPLEMENTARY MATERIALS

science.org/doi/10.1126/science.abi7687
Materials and Methods
Supplementary Text
Figs. S1 to S18
Table S1
References (36–45)

1 April 2021; accepted 29 July 2021
10.1126/science.abi7687

Ultrahigh energy storage in superparaelectric relaxor ferroelectrics

Hao PanShun LanShiqi XuQinghua ZhangHongbao YaoYiqian LiuFanqi MengEr-Jia GuoLin GuDi YiXiao Renshaw WangHoubing HuangJudith L. MacManus-DriscollLong-Qing ChenKui-Juan JinCe-Wen NanYuan-Hua Lin

Science, 374 (6563), • DOI: 10.1126/science.abi7687

Minimal domains for maximum energy

Dielectric capacitors are important electronic components that can store energy, at least for a short period of time. Pan *et al.* used phase-field simulations to help determine the right combination of bismuth iron oxide, barium titanium oxide, and samarium doping that is likely to generate a material with excellent dielectric properties (see the Perspective by Chu). The simulations guide a set of experimental measurements showing this system can produce a very high-energy storage by breaking down polar domains to the nanometer scale. These materials could be useful for high-power applications and to suppress failure. —BG

View the article online

<https://www.science.org/doi/10.1126/science.abi7687>

Permissions

<https://www.science.org/help/reprints-and-permissions>

Use of think article is subject to the [Terms of service](#)

Science (ISSN) is published by the American Association for the Advancement of Science. 1200 New York Avenue NW, Washington, DC 20005. The title *Science* is a registered trademark of AAAS.

Copyright © 2021 The Authors, some rights reserved; exclusive licensee American Association for the Advancement of Science. No claim to original U.S. Government Works